

The Power Spectrum of the Thermal Sunyaev-Zeldovich Effect

George Efstathiou^{1,2} and Fiona McCarthy^{3,1,4}

[1] *Kavli Institute for Cosmology Cambridge, Madingley Road, Cambridge, CB3 0HA, UK.*

[2] *Institute of Astronomy, Madingley Road, Cambridge, CB3 0HA, UK.*

[3] *DAMTP, Centre for Mathematical Sciences, University of Cambridge, Wilberforce Road, Cambridge CB3 0WA, UK.*

[4] *Center for Computational Astrophysics, Flatiron Institute, 162 5th Avenue, New York, NY 10010 USA.*

16 May 2025

ABSTRACT

The power spectrum of unresolved thermal Sunyaev-Zeldovich (tSZ) clusters is extremely sensitive to the amplitude of the matter fluctuations. This paper presents an analysis of the tSZ power spectrum using temperature power spectra of the cosmic microwave background (CMB) rather than maps of the Compton y -parameter. Our analysis is robust and insensitive to the cosmic infrared background. Using data from *Planck*, and higher resolution CMB data from the Atacama Cosmology Telescope and the South Pole Telescope, we find strong evidence that the tSZ spectrum has a shallower slope and a much lower amplitude at multipoles $\ell \gtrsim 2000$ compared to the predictions of the baseline FLAMINGO hydrodynamic simulations of the Λ CDM cosmology. Recent results on CMB lensing, cross-correlations of CMB lensing with galaxy surveys and full shape analysis of galaxies and quasars from the Dark Energy Spectroscopic Instrument suggests that this discrepancy cannot be resolved by lowering the amplitude of the matter fluctuations. An alternative possibility is that the impact of baryonic feedback in the baseline FLAMINGO simulations is underestimated.

Key words: cosmology: cosmic background radiation, cosmological parameters, galaxies:clusters:

1 INTRODUCTION

The thermal Sunyaev-Zeldovich (tSZ) is caused by the inverse Compton scattering of cosmic microwave background photons with the electrons in the hot atmospheres of groups and clusters of galaxies (Sunyaev & Zeldovich 1972). The tSZ effect can be disentangled from the primordial black-body CMB anisotropies via its distinctive spectral signature, offering a potentially powerful probe of structure formation. Furthermore, it has long been known that the integrated tSZ signal from clusters depends sensitively on the amplitude of the matter fluctuation spectrum (Cole & Kaiser 1988; Komatsu & Kitayama 1999; Komatsu & Seljak 2002).

Let us define the Compton y -parameter seen on the sky in direction \hat{l} by the line-of-sight integral

$$y = \int n_e \frac{kT_e}{m_e c^2} \sigma_T dl, \quad (1)$$

where n_e and T_e are the electron density and temperature and σ_T is the Thomson cross-section. At frequency ν , the tSZ effect produces a change in the thermodynamic temperature of the CMB of

$$\frac{\Delta T}{T_{\text{CMB}}} = f(x)y, \quad (2a)$$

where¹

$$f(x) = x \frac{(e^x + 1)}{(e^x - 1)} - 4, \quad x \equiv \frac{h_p \nu}{kT_{\text{CMB}}}, \quad (2b)$$

(see e.g. Carlstrom et al. 2002, for review of the tSZ effect).

Komatsu & Seljak (2002) made reasonable assumptions concerning the pressure profiles of clusters (discussed in more detail below) and integrated over the cluster mass function to make theoretical predictions for the tSZ power spectrum, $C_\ell^{yy\text{pred}}$, expected in a Λ CDM cosmology. They found the following scaling with cosmological parameters:

$$C_\ell^{yy\text{pred}} \propto \sigma_8^{8.1} \Omega_m^{3.2} h^{-1.7}, \quad (3)$$

where σ_8 is the root mean square linear amplitude of the matter fluctuation spectrum in spheres of radius $8h^{-1}\text{Mpc}$ extrapolated to the present day, Ω_m is the present day matter density in units of the critical density and h is the value of the Hubble constant H_0 in units of $100 \text{ km s}^{-1} \text{ Mpc}^{-1}$. We can rewrite Eq. 3 as

$$C_\ell^{yy\text{pred}} \propto (S_8 \omega_m^{-0.1})^{8.1}, \quad (4)$$

¹ We use the notation h_p for the Planck constant to distinguish it from the dimensionless Hubble parameter.

where S_8 is the parameter combination $S_8 = \sigma_8(\Omega_m/0.3)^{0.5}$, which is accurately measured in cosmic shear surveys, and $\omega_m = \Omega_m h^2$ measures the physical density of matter in the Universe. The parameter ω_m is determined very accurately from the acoustic peak structure of the CMB temperature and polarization power spectra in the minimal 6-parameter Λ CDM cosmology and is insensitive to simple extensions beyond Λ CDM (Planck Collaboration et al. 2020b, hereafter P20). Thus the amplitude of the tSZ power spectrum is expected to depend sensitively on the S_8 parameter.

Observations of the tSZ effect therefore have a bearing on the discrepancy between the value of S_8 determined from the CMB and the values inferred from weak galaxy lensing surveys (Hikage et al. 2019; Asgari et al. 2021; Amon et al. 2022; Secco et al. 2022, e.g.) which has become known as the ‘ S_8 -tension’. The discrepancy is at the level of $\sim 1.5 - 3\sigma$, depending on the specific weak lensing survey, choices of scale-cuts, model for intrinsic alignments and assumptions concerning baryonic physics (Amon & Efstathiou 2022; Preston et al. 2023; Dark Energy Survey and Kilo-Degree Survey Collaboration et al. 2023). Although this is not strongly significant, an S_8 tension has been reported since the early days of weak lensing surveys (Heymans et al. 2012; MacCrann et al. 2015). The question of whether cosmic shear measurements require new physics beyond Λ CDM is unresolved and remains a topic of ongoing research.

This paper is motivated by the analysis of the **FLAMINGO** suite of cosmological hydrodynamical simulations presented in McCarthy et al. (2023) (hereafter M23). (See Schaye et al. (2023) for an overview of the **FLAMINGO** project and a description of the simulations used in M23.) The main aim of M23 is to assess the impact of baryonic feedback of various physical quantities sensitive to the S_8 parameter, including galaxy shear two-point statistics and the tSZ power spectrum. The ‘sub-grid’ feedback prescriptions used in the baseline **FLAMINGO** simulations are constrained to match the present day galaxy stellar mass function and the gas fractions observed in groups and clusters of galaxies. One of their most striking results concerns the tSZ power spectrum. They argue that the tSZ power spectrum is dominated by massive clusters and is therefore insensitive to small variations of the baryonic feedback model around the baseline. Yet their simulation predictions based on a *Planck*-like Λ CDM cosmology have a much higher amplitude than the tSZ power spectrum inferred by Bolliet et al. (2018) (hereafter B18) from the *Planck* map of the tSZ effect (Planck Collaboration et al. 2016a) and with the tSZ amplitude inferred at high multipoles from observations with the South Pole Telescope (SPT) (Reichardt et al. 2021). Since the amplitude of the tSZ signal is strongly dependent on the S_8 parameter (Equ. 4) M23 conclude that a new physical mechanism is required to lower the value of S_8 below that of the *Planck* Λ CDM cosmology.² This is potentially an important result since it presents evidence for an S_8 tension independent of

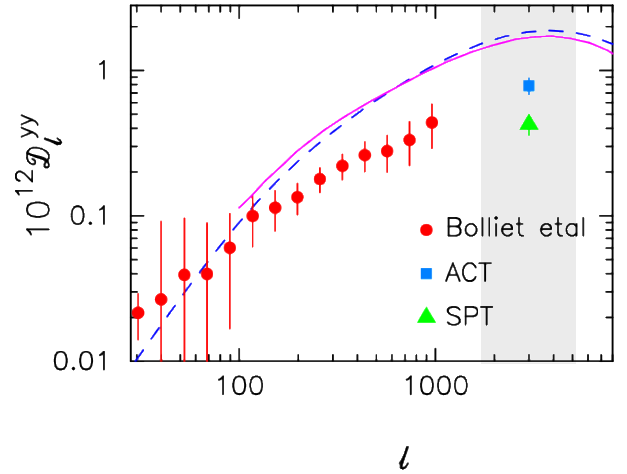


Figure 1. The red points show estimates of the tSZ power spectrum from B18, together with 1σ errors. The blue and green points show the amplitudes of template tSZ power spectra at $\ell = 3000$ inferred from high resolution ground based CMB power spectra measured by the ACT and SPT collaborations (Choi et al. 2020; Reichardt et al. 2021). The grey band is included to highlight the fact that the ACT and SPT measurements are model dependent amplitudes rather than measurements at $\ell = 3000$. The purple line shows the tSZ spectrum determined from a **FLAMINGO** simulation of the *Planck* Λ CDM cosmology assuming their default ‘sub-grid’ parameters. The dashed blue line shows a simple one-halo model described in the text that is designed to match the **FLAMINGO** results.

cosmic shear surveys using a statistic that is claimed to be insensitive to baryonic feedback processes.

We reassess the conclusions of M23 in this paper. As discussed in Sect. 2 and in more detail in Sect. 3, power spectra computed from *Planck*-based Compton y -maps are strongly contaminated by several components which must be known and subtracted to high accuracy to infer a tSZ power spectrum. Section 4 presents a much simpler power-spectrum based approach applied to *Planck* data. Our analysis is designed to isolate the unresolved tSZ effect and the white noise contribution from radio point sources from the cosmic infrared background (CIB), which is poorly known at frequencies $\lesssim 217$ GHz. The amplitude of the radio source power spectrum can be constrained from deep number counts, breaking the degeneracy between the tSZ and radio source power spectra. We also present results of power spectrum analyses at high multipoles using data from SPT and the Atacama Cosmology Telescope (ACT) (Sievers et al. 2013; Das et al. 2014; Choi et al. 2020). Finally, we combine data from *Planck*, ACT and SPT to reconstruct the shape of the tSZ power spectrum over the multipole range $\ell \sim 200$ –7000. Our conclusions are summarized in Sec. 5.

² Note that this discrepancy was first highlighted by McCarthy et al. (2014) who showed, using an early series of numerical hydrodynamic simulations, that the tSZ power spectrum predicted assuming the *Planck* cosmology had a higher amplitude than inferred from ACT and SPT (Reichardt et al. 2012; Sievers et al. 2013).

2 THE MOTIVATION FOR THIS PAPER

Figure 1 is based on Fig. 5 from M23. The red points show the tSZ power spectrum inferred by B18³ from the *Planck* all-sky maps of the Compton y -parameter (which we will refer to as y -maps) available from the Planck Legacy Archive⁴ (PLA) (Planck Collaboration et al. 2016a).

The error bars show 1σ errors as reported in B18. The purple line shows the FLAMINGO results from M23 for a simulation of the *Planck* Λ CDM cosmology using their default feedback parameters (solid green line in the upper right hand plot in Fig. 5 from M23). The two points at multipoles of $\ell \approx 3000$ show the amplitude of the tSZ power spectrum inferred from SPT (Reichardt et al. 2021) and from ACT (Choi et al. 2020). These measurements at high multipoles are fundamentally different from the B18 analysis since they are based on fits of a parametric foreground model to temperature power spectra whereas B18 infer the tSZ power spectrum from y -maps. Although the high-multipole results are usually plotted at $\ell = 3000$, as in Fig. 1, it is important to emphasise that these points are not measurements of the tSZ signal at $\ell = 3000$. They give the amplitude of an assumed tSZ template spectrum at $\ell = 3000$. To emphasise this difference, we have superimposed a shaded area over these points to signify qualitatively that a range of angular scales contributes to the ACT and SPT measurements. Note further that the ACT and SPT amplitudes appear to differ by $\sim 2\sigma$. The consistency of the ACT and SPT tSZ results and the exact multipole ranges sampled by these experiments will be made more precise in Sect. 4.

One can see that the FLAMINGO curve fails to match the B18 points by a wide margin. M23 also ran a set of simulations, labelled LS8, which have *Planck*- Λ CDM parameters except that the amplitude of the linear fluctuation spectrum was reduced to give a low value of $S_8 = 0.766$ at the present day to match the weak lensing results reported by Amon et al. (2023). The LS8 cosmology clips the upper ends of the B18 error bars and so provides a better fit to the data than the *Planck* Λ CDM cosmology. The LS8 model moves in the right direction but does not lower the tSZ amplitude enough to explain the B18 results. Furthermore, the LS8 model fails to match the ACT and SPT point by many standard deviations. Evidently, simply lowering the amplitude of the fluctuation spectrum to match weak lensing measurements cannot reconcile the simulations with the ACT and SPT data points shown in Fig. 1.

The dotted blue line in Fig. 1 shows a one-halo model (Komatsu & Seljak 2002) for the tSZ power spectrum computed as described in Efstathiou & Migliaccio (2012) for the *Planck*-like Λ CDM cosmological parameters adopted in M23. The electron pressure profile was assumed to follow the ‘universal’ pressure profile of Arnaud et al. (2010)

$$P_e(x) = 1.88 \left[\frac{M_{500}}{10^{14} h^{-1} M_\odot} \right]^{0.787} p(x) E(z)^{\frac{8}{3}-\epsilon} h^2 \text{eV cm}^{-3}, \quad (5)$$

³ Specifically, B18 use a cross-spectrum of the Needlet Internal Linear Combination (NILC Delabrouille et al. 2009) y -map constructed from the first half of the *Planck* data and the Modified Internal Linear Combination Algorithm (MILCA Hurier et al. 2013) y -map from the second half of the *Planck* data.

⁴ <https://pla.esac.esa.int>

where

$$p(x) = \frac{P_0 h^{-3/2}}{(c_{500} x)^\gamma (1 + [c_{500} x]^\alpha)^{(\beta-\gamma)/\alpha}}, \quad (6)$$

with the parameters $P_0 = 4.921$, $c_{500} = 1.177$, $\gamma = 0.3081$, $\alpha = 1.051$, $\beta = 5.4005$ and $x = r/R_{500}$. Here R_{500} is the radius at which the cluster has a density contrast of 500 times the critical density at the redshift of the cluster, M_{500} is the mass of the cluster within R_{500} , and the function $E(z)$ in (5) is the ratio of the Hubble parameter at redshift z to its present value,

$$E(z) = [(1 - \Omega_\Lambda)(1 + z)^3 + \Omega_\Lambda]^{1/2}. \quad (7)$$

The scaling $E(z)^{8/3}$ in Eq. (5) assumes self-similar evolution and the parameter ϵ was introduced by Efstathiou & Migliaccio (2012) to model departures from self-similar evolution. The Arnaud et al. (2010) pressure profile with $\epsilon = 0$ provides a good match to the pressure profiles of massive clusters in the FLAMINGO simulations (see Fig. 3 of Braspennig et al. 2023). As can be seen from Fig. 1, this simple one-halo model (plotted as the dashed blue line) gives a very good match to the tSZ power spectrum measured in the FLAMINGO simulation. Notice also that there is no mass bias parameter involved in this comparison because the simulations measure the masses of clusters directly.

Following Komatsu & Seljak (2002), the tSZ power spectrum is given by

$$D_\ell^{tSZ} = \frac{\ell(\ell+1)}{2\pi} \int dz \frac{dV}{dz d\Omega} \int \frac{dn}{dM} dM |y_\ell(M, z)|^2, \quad (8a)$$

where $(dn/dM)dM$ is the halo mass function⁵ and in the small angle approximation y_ℓ is given by the following integral over the pressure profile:

$$y_\ell = \frac{\sigma_T}{m_e c^2} \frac{4\pi R_{500}}{\ell_{500}^2} \int dx x^2 \frac{\sin(\ell x / \ell_{500})}{(\ell x / \ell_{500})} P_e(x), \quad (8b)$$

where ℓ_{500} is the multipole corresponding to the angular size subtended by R_{500} at the redshift of the cluster.

The contribution to the tSZ power spectrum as a function of multipole, cluster virial mass and redshift is shown in Fig. 2. At $z \lesssim 0.5$, this figure shows similar behaviour to Fig. 3 from (McCarthy et al. 2014), which is based on the cosmo-OWLS simulations. For the multipoles relevant to *Planck* ($\ell \sim 200 - 500$, see below) shown approximately by the pink shaded bands, the tSZ power spectrum is dominated by clusters at low redshift ($z \lesssim 0.5$) with virial masses $M_V \gtrsim 10^{14.5} M_\odot$. M23 argue that baryonic feedback processes in such massive clusters are unlikely to drastically alter their pressure profiles. At the higher multipoles probed by ACT and SPT ($\ell \sim 2000 - 3000$) indicated by the blue bands, the tSZ power spectrum probes lower mass clusters at higher redshifts (Komatsu & Seljak 2002) and is therefore more sensitive to feedback processes and departures from self-similarity. This is illustrated in Fig. 2, where we have shown the steep decline in the power spectrum at high redshift if the evolution parameter in Eq. 5 is set to $\epsilon = 1$ instead of the self-similar value $\epsilon = 0$. However, even at high multipoles ~ 3000 , M23 conclude that plausible variations in the FLAMINGO feedback model cannot reproduce the

⁵ As in Efstathiou & Migliaccio (2012), we use the Jenkins et al. (2001) parameterization of the halo mass function.

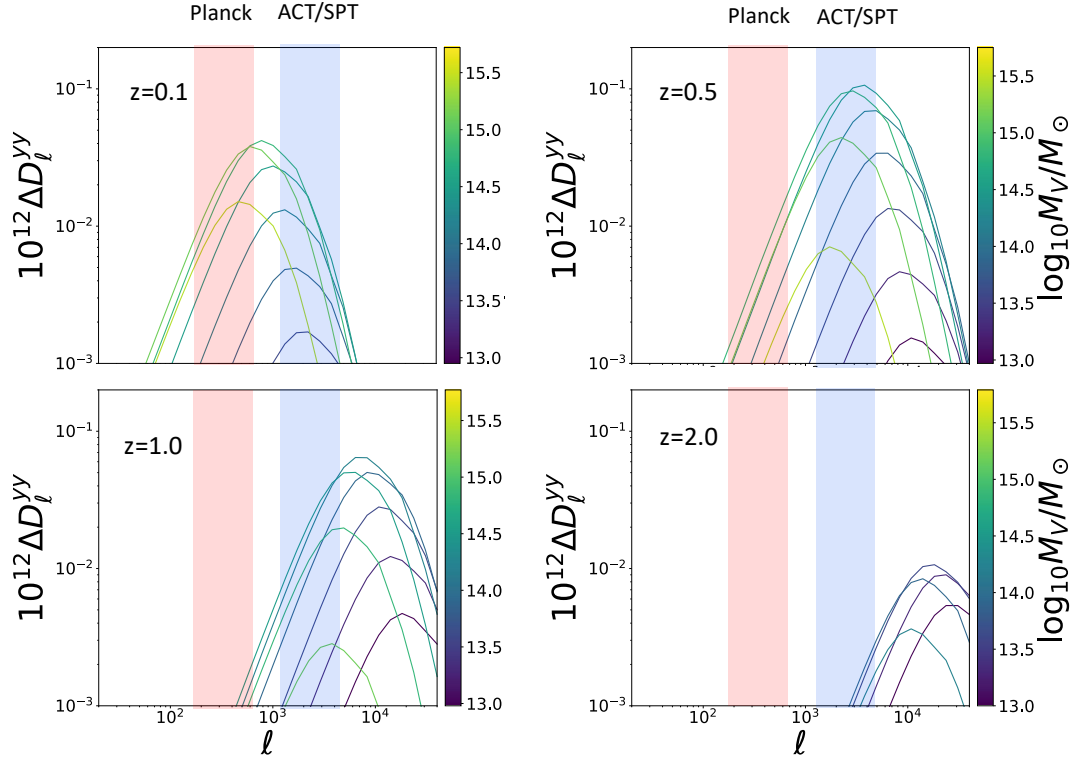


Figure 2. The contribution to the tSZ power spectrum, computed from the one-halo model described in the text, plotted as a function of virial cluster mass M_V (measured in M_\odot), redshift and multipole. The evolution parameter ϵ in Eq. 5 has been set to $\epsilon = 1$ in this example, leading to the sharp decline in power at $z \gtrsim 1$ (see Sect 5). The shaded regions show the approximate range of multipoles probed by *Planck*, ACT and SPT. .

tSZ measurements reported by ACT and SPT assuming the *Planck* Λ CDM cosmology. The main purpose of this paper is to critically reassess the reliability the tSZ measurements plotted in Fig. 1.

3 ANALYSIS OF Y-MAPS

Figure 3 shows the decomposition of the NILC×MILC y-map cross spectrum analysed by B18 into various components. The total power spectrum is shown by the green points. The red points show the tSZ power spectrum computed by B18 (as plotted in Fig. 1) after subtraction of the CIB, radio sources and resolved clusters. As can be seen, the inferred tSZ is a small fraction of the total signal over the entire multipole range shown in Fig. 3 and is therefore extremely sensitive to the assumed shapes of the contaminant power spectra. B18 adopted template shapes from *Planck* Collaboration et al. (2016a) folded through the NILC and MILC weights. The clustered CIB component and IR point source amplitudes are from the models of Béthermin et al. (2012) and the radio point source amplitudes are from the models of Tucci et al. (2011). The model for the tSZ spectrum contributed by clusters resolved by *Planck*, plotted as the dashed green line in Fig. 3 is described in *Planck* Collaboration et al. (2016a). There are significant uncertainties associated with the template spectra. Figure 3 implies

that the CIB is the dominant contaminant, yet very little is known about the amplitude and shape of the CIB power spectrum at 100 and 143 GHz and it is dangerous to rely on the models of Béthermin et al. (2012)⁶.

In addition to the y-maps constructed by the *Planck* collaboration, y-maps have been constructed from the *Planck* data by other authors (e.g. Hill & Spergel 2014; Tanimura et al. 2022; Chandran et al. 2023; McCarthy & Hill 2024) and also from combinations of ACT, SPT and *Planck* maps (Madhavacheril et al. 2020; Bleem et al. 2022; Coulton et al. 2024). The blue and red points in Fig. 4 show the NILC and MILC half-ring cross-spectra computed from the y-maps described by *Planck* Collaboration et al. (2016a)⁷. These were computed using the apodised 70% sky masks available from the PLA with no corrections for point sources and extended sources. As reported in *Planck* Collaboration et al. (2016a), the amplitude of the MILC power spectrum is nearly a factor of two higher than that of the NILC power spectrum showing that the contamination is sensitive to the map making technique.

⁶ Even at high frequencies of 350 μ m and 500 μ m (860 and 600 GHz) when most of the CIB is resolved by Herschel (Viero et al. 2013), the Béthermin et al. (2012) models fail at multipoles $\gtrsim 2000$ (see Mak et al. (2017)).

⁷ downloaded from https://irsa.ipac.caltech.edu/data/Planck/release.2/all-sky-maps/ysz_index.html.

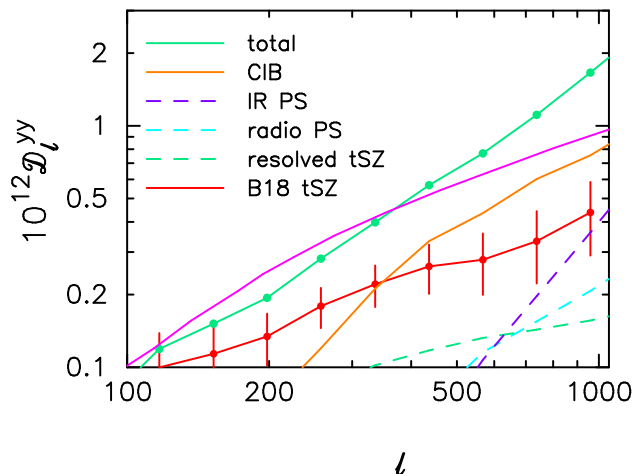


Figure 3. The green points show the power spectrum of the NILC x MILC y-map cross spectrum analysed by B18. The figure shows the contributions from the clustered CIB, infrared point sources, radio sources, resolved SZ clusters and unresolved tSZ determined by B18 by fitting template power spectra to the green points. The B18 tSZ power spectrum is a subdominant component of the total power spectrum over most of the multipole range shown in the figure. The purple line shows the tSZ power spectrum from the FLAMINGO simulation of the Λ CDM cosmology (as plotted in Fig. 1).

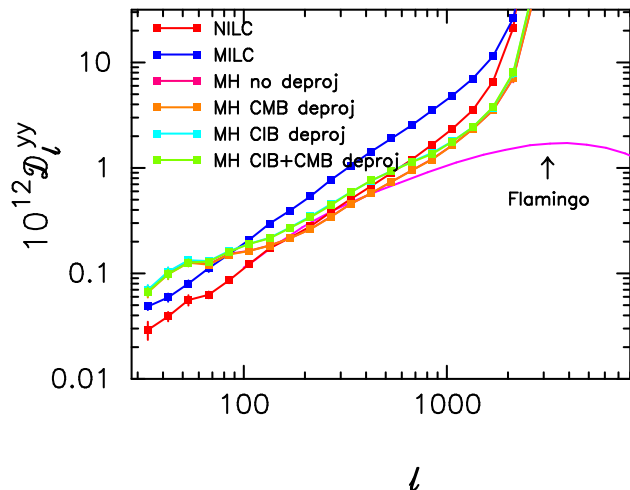


Figure 4. The curves labelled NILC and MILC show half-ring cross spectra of the *Planck* y-maps. The curves labelled MH show half-ring cross spectra of y-maps constructed by McCarthy & Hill (2024) with no deprojection (as in standard NILC) and with additional constraints applied to deproject the CMB, CIB and CMB+CIB. Note that the pink ‘MH no deproj’ points lie almost exactly under the ‘MH CMB deproj’ points, and the cyan ‘MH CIB deproj’ points lie under the ‘MH CIB+CMB deproj’ points.

The remaining points in Fig 4 show cross-power spectra of half-ring split y-maps constructed by (McCarthy & Hill 2024, hereafter MH24)⁸. These were computed using the identical sky masks as those used to compute the *Planck* MILC and NILC spectra shown in the figure. MH24 applied a NILC algorithm to the *Planck* PR4 maps (Planck Collaboration et al. 2020c) but with constraints to deproject various components. The spectrum labelled ‘MH no deprojection’ shows the results for the standard y-map ILC method (similar to the *Planck* NILC algorithm), while the remaining spectra show results for deprojection of the CMB, CIB, and CIB+CMB components respectively. All of these have similar amplitudes. In addition, MH24 applied a moment-based deprojection (based on the work of Chluba et al. (2017)) which accounts for small variations in the spectral index of the CIB, though at the expense of increasing the effective noise levels in the reconstructed y-maps.

To gain insight into the contamination of the y-maps, we tested the MH24 algorithms against simulations with known foregrounds. The *Planck*-like simulations include extragalactic components from Websky (Stein et al. 2020) and Galactic components from PySM3 (Thorne et al. 2017). The extragalactic components included are the lensed CMB and kSZ (which are included as blackbody components) and the CIB (as described by Stein et al. 2020) and radio point sources (from Li et al. 2022). The simulations were produced at the *Planck* frequencies of 30, 44, 70, 100, 143, 353, and 545 GHz, but note that the Websky CIB is not provided at frequencies lower than 143 GHz and so for the lower frequency channels we simply rescale the CIB from 143 GHz using a modified-black-body emission law with dust temperature 20K and spectral index 1.6 (see MH24; these parameters are assumed in the deprojection of the CIB). The Galactic components included from PySM3 are thermal dust (s1), synchrotron radiation (s1), anomalous microwave emission (a1), and free-free emission (f1), where the specification in brackets identifies the specific PySM3 model (we refer the reader to the PySM3 documentation for details of these models). At each frequency, we convolve with a *Planck*-like beam and create two realizations of Gaussian white noise (at a level appropriate for the PR4 *Planck* maps), which we add to the simulated sky signal to emulate two independent splits.

We apply a NILC algorithm similar to that of MH24 to the each set of multifrequency splits using `pyilc`⁹ (MH24).¹⁰ We save the computed ILC weights and apply them separately to each of the components, to assess the level of contamination of each component in the final map. We do this for the four deprojection options: the minimum-variance ‘no deprojection’ version; a CMB-deprojected version; and CMB+CIB and CMB+CIB+ $\delta\beta$ -deprojected version following the constrained ILC framework described in MH24 (see also Chen & Wright 2009; Remazeilles et al. 2011).

⁸ https://users.flatironinstitute.org/~mccarthy/ymaps_PR4_McH23/ymap_standard.

⁹ <https://github.com/jcolinhill/pyilc>

¹⁰ We note that there is a slight difference in the needlet basis used with respect to MH24, although we expect the conclusions to be nearly identical. The needlet basis used in MH24 was a set of Gaussian needlets which followed the *Planck* tSZ NILC analysis (as described in MH24); the simulations described here use a cosine needlet basis.

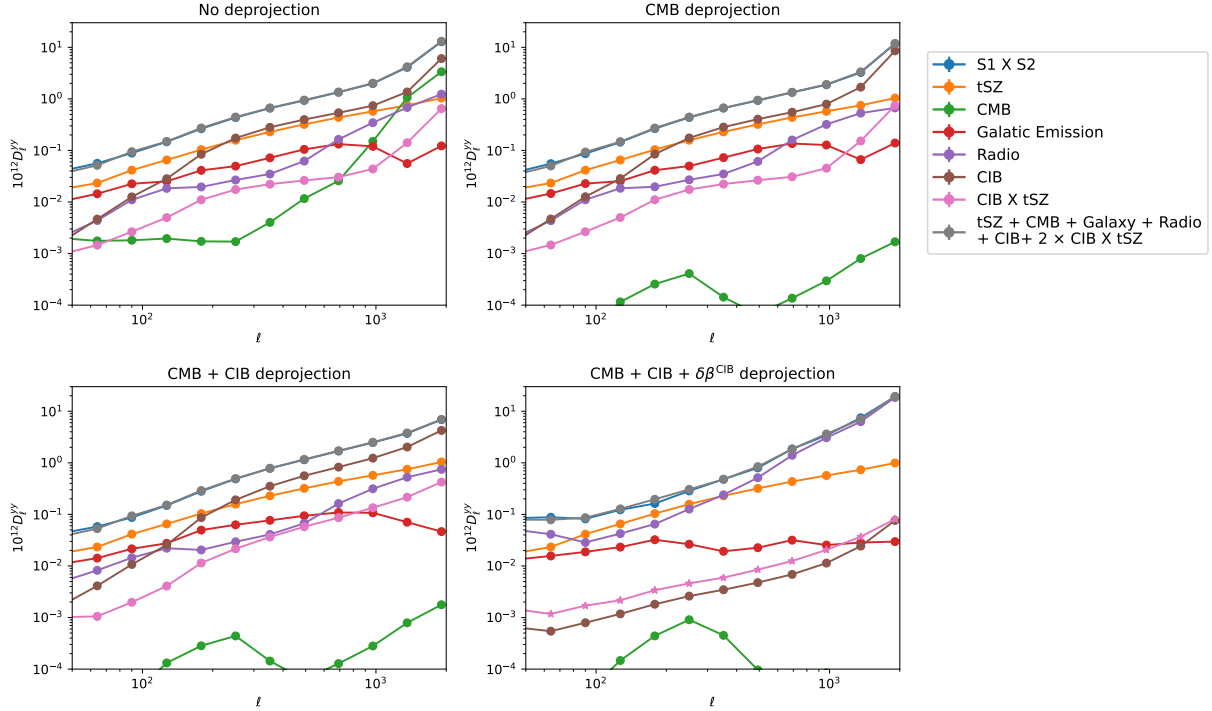


Figure 5. Contribution of each component to the measured power spectrum of a simulated NILC y -map *Planck*-like analysis. The blue points show the measured split power spectrum of our simulations, and the various coloured points show the contribution of the components, with the true tSZ signal in orange, the CIB in brown, and radio point sources in purple. When the CIB is minimized by deprojecting the CIB and its first moment (bottom right), the radio contribution increases to compensate, illustrating the difficulty of simultaneously cleaning all of the foregrounds.

By applying the weights separately to each component, we can assess how much of each foreground leaks into the final maps. In Figure 5 we show the measured power spectra of the NILC map and of each component, measured on the area of sky defined by the apodized *Planck* 70% sky mask. From the ‘no-deprojection’ and ‘CMB-deprojection’ plots (top row of Figure 5) it is clear that the tSZ contribution (orange lines) only accounts for $\sim 50\%$ of the power spectrum of the full map, with the CIB (brown lines) the main contaminant, along with a Galactic contribution on the largest scales (red lines). Interestingly, the deprojection of the CIB alone (bottom left row) does not remove a significant amount of CIB power. When we deproject both the CMB and the first moment of the CIB (indicated by CIB + $\delta\beta^{\text{CIB}}$ deprojection, on the bottom right) we see that the CIB contribution is significantly decreased; however this is at the expense of a compensatory increase in radio source power (purple lines). In this case, the y -map power spectrum is similar to the CMB subtracted 100 GHz power spectrum analysed in the next Section.

In summary, these simulations demonstrate that y -maps are heavily contaminated by other components and that the nature of the contaminants is sensitive to the way in which the y -maps are constructed. This is the motivation for seeking another way of extracting the tSZ power spectrum.

4 THE TSZ AMPLITUDE INFERRED FROM THE TEMPERATURE POWER SPECTRUM

An alternative way of estimating the tSZ effect is to fit a parametric foreground model to CMB power spectra measured at several frequencies. This type of analysis has been used to remove foreground contributions from the *Planck*, ACT and SPT temperature power spectra (e.g. Dunkley et al. 2013; Planck Collaboration et al. 2014b, 2020b; Choi et al. 2020; Reichardt et al. 2021). The tSZ amplitude inferred from these investigations, including from *Planck*, is consistently lower than the predictions of the FLAMINGO simulations.¹¹

The best fit foreground model (see e.g. Fig. 32 of Planck Collaboration et al. 2020a) illustrates the difficulty of extracting an accurate tSZ amplitude either from y -maps or from power spectra. The tSZ effect in the *Planck* data dominates over other foreground contributions only at frequencies of ~ 100 GHz and only at multipoles $\lesssim 500$. At lower frequencies radio sources dominate and at higher frequencies the clustered CIB and Poisson contributions from radio and infrared sources dominate. In addition, Galactic foregrounds become significant at low multipoles if large areas of sky are used. Power spectrum analyses face similar difficulties to the map-based analyses described in the previous

¹¹ It is for this reason that the *Planck* cosmological parameter papers used the Efstathiou & Migliaccio (2012) template with $\epsilon = 0.5$ (see Eq. 5) to flatten the tSZ template compared to the FLAMINGO template of Fig. 1.

section. The tSZ amplitude is small and cannot be extracted without making assumptions concerning the shapes of the power spectra of the contaminants, particularly the clustered CIB. However, there is an advantage in working in the power spectrum domain because one can restrict the range of frequencies to reduce the impact of contaminants with poorly known power spectra. The goal of this section is to present power spectrum analyses of *Planck*, ACT and SPT that are insensitive to the CIB. We consider the *Planck* power spectra in Sect. 4.1 and then present slightly different analyses in Sect. 4.2 tailored to the high multipoles probed by ACT and SPT. We present a (template-free) reconstruction of the tSZ power spectrum from these experiments in Sect. 4.3.

4.1 Analysis of Planck spectra

The aim of this subsection is to reduce systematic biases in measurements of the tSZ power spectrum. To achieve this, we first restrict the sky area that is analyzed by applying the apodized 50% sky mask available from the PLA¹². This is a smaller sky area than is used for cosmological parameter analysis (see e.g. EG21 who use 80% sky masks), but is chosen because in this paper reduction of biases caused by Galactic emission is a more important consideration than increasing the signal-to-noise of the power spectra. In addition to the sky mask, we mask sources with 100 GHz point source flux density (PSFLUX) greater than 400 mJy listed in the Second *Planck* Catalogue of Compact Sources (PCCS2 [Planck Collaboration et al. 2016b](#)). At this flux limit, the PCCS2 is $\sim 98\%$ complete at 100 GHz (see Fig. 7 of PCCS2). As described below, this high degree of completeness allows us to constrain the Poisson point source amplitude by using faint number counts of radio sources at 100 GHz. The point source mask was constructed by applying a sharp symmetric weight function $w_{\text{PS}}(\theta)$ as a function of the angular distance θ relative to the position of each source,

$$w_{\text{PS}}(\theta) = 1 - e^{-(\theta/\sigma_{\text{PS}})^{15}},$$

where $\sigma_{\text{PS}} = 40'$. To this mask we add the *Planck* extended object mask and excise a (lightly apodised) disc of radius 2.4° centred on the position of the Coma cluster at Galactic coordinates $\ell = 58.6^\circ$, $b = 87.96^\circ$. The resulting mask is shown in Fig. 6.

We focus on the 100 GHz power spectrum, since the main contributors at this frequency are the primary CMB, tSZ and radio sources¹³. Throughout this Section, we com-

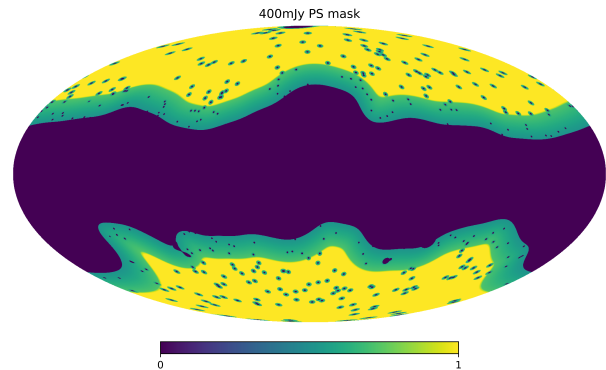


Figure 6. Mask applied to the *Planck* maps for the analysis described in Sect. 4.1.

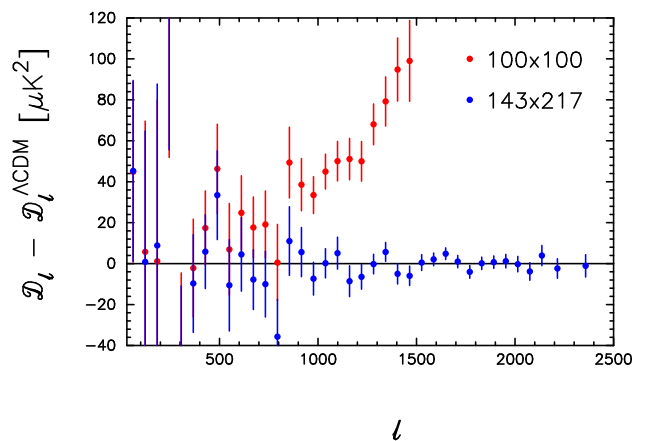


Figure 7. The 545 GHz dust-cleaned 100×100 cross spectrum (red points) and dust-cleaned 143×217 cross spectrum (blue points) with the best fit Λ CDM spectrum from RGE22 subtracted. The spectra were computed using the 400 mJy 100GHz point source and extended object mask shown in Fig. 6. A small correction was applied to the 143×217 cross spectrum (see Eq. 9) to remove extragalactic foregrounds at high multipoles. Error bars ($\pm 1\sigma$) on the bandpowers were computed from the *CamSpec* covariance matrices.

pute cross spectra from the PR4 *Planck* A and B maps ([Planck Collaboration et al. 2020c](#)), following the *CamSpec* analysis described by [Efstathiou & Gratton \(2021\)](#) (hereafter EG21) and [Rosenberg et al. \(2022\)](#) (hereafter RGE22). The amplitude of the tSZ contribution to the 100 GHz power spectrum is expected to be less than $10 \mu\text{K}^2$ compared to the amplitude of $\sim 6000 \mu\text{K}^2$ at $\ell \sim 200$ of the primary CMB. To detect such a small effect, it is necessary to use the *Planck* data themselves to estimate the contribution from primary CMB in order to eliminate cosmic variance. In our analysis, we subtract the primary CMB using a 545 GHz dust-cleaned 143×217 GHz cross-spectrum computed using the sky mask shown in Fig. 6. The dust cleaning is performed in the power spectrum domain as discussed in Sect. 7.3 of EG21. The dust cleaning removes most of the CIB in the 143×217 spectrum in addition to Galactic dust emission, leaving a small foreground contribution at high multipoles (see Fig. 11.4 of

¹² Planck Legacy Archive: <https://pla.esac.esa.int/#home>.

¹³ The CIB model of [Béthermin et al. \(2012\)](#), normalized to the best fit CIB amplitude at 217 GHz determined from a combined CMB+foreground power spectrum analysis to the *Planck* spectra over the frequency range 100-217 GHz, has an amplitude of $D_{\ell=500} = 0.25 \mu\text{K}^2$ (see Fig. 9.2 of ([Efstathiou & Gratton 2021](#))). This is much smaller than the best fit tSZ amplitude of $D_{\ell=500} \sim 6.9 \mu\text{K}^2$ inferred at 100 GHz (see Fig. 8). We therefore ignore the CIB contribution at 100 GHz. The *Planck* lower frequencies are dominated by radio sources. In the future, high resolution ground based observations in the frequency range 30-100 GHz ([Ade et al. 2019](#)) will provide useful information on the tSZ effect.

EG21). The best fit base TTTEEE Λ CDM power spectrum of RGE22 is accurately reproduced by subtracting the following power law from the dust cleaned 143×217 power spectrum:

$$D_\ell^{143 \times 217 \text{corr}} = D_\ell^{143 \times 217} - 12.295(\ell/1500)^{1.701} \mu\text{K}^2. \quad (9)$$

This is close to the best fit foreground model in the fits described in REG but differs slightly because REG used different point source masks at 143 and 217 GHz. The residuals of $D_\ell^{143 \times 217 \text{corr}}$ relative to the best fit Λ CDM model are shown by the blue points in Fig. 7.

The red points in Fig. 7 show the residuals for the dust-cleaned 100×100 cross spectrum with no correction for foreground components. At low multipoles $\ell \lesssim 500$, the 100×100 and 143×217 spectra track each other to within $10 - 20 \mu\text{K}^2$ because the errors at these low multipoles are dominated by cosmic variance. At higher multipoles, the spectra diverge as radio sources become significant in the 100×100 spectrum.

The difference between these two spectra are shown in the upper panel of Fig. 8. We have split the figure into two parts so that one can see visually the best fit tSZ contribution at low multipoles. The errors on the difference, $\Delta D_\ell = D_\ell^{100 \times 100} - D_\ell^{143 \times 217}$ are computed from the **CamSpec** covariance matrices which include small Gaussian contributions from the best fit foreground model of Eqs. 9 and 12. We also added a trispectrum contribution to the covariance matrix (arising from the angular extent of nearby clusters) of the bandpowers plotted in Fig. 7

$$M_{bb'}^{\text{Tr}} = \frac{T_{bb'}}{4\pi f_{\text{sky}}}, \quad T_{bb'} = \sum_{\ell \in b} \sum_{\ell' \in b'} \frac{T_{\ell\ell'}}{N_b N_{b'}} \quad (10a)$$

where N_b is the number of multipoles contributing to bandpower b ,

$$T_{\ell\ell'} = \frac{\ell(\ell+1)\ell'(\ell'+1)}{4\pi^2} \int dz \frac{dV}{dz d\Omega} \int \frac{dn}{dM} dM |y_\ell(M, z)|^2 |y_{\ell'}(M, z)|^2, \quad (10b)$$

(Komatsu & Seljak 2002; Shaw et al. 2009; Hill & Pajer 2013; Bolliet et al. 2018) and $y_\ell(M, z)$ is given in Eq. 8b. To evaluate this expression we adopt the fiducial tSZ model that was used to produce the dashed curve in Fig. 1 and set $f_{\text{sky}} = \sum w_i^2 (\Omega_i/4\pi) = 0.396$, where the sum extends over all map pixels each of solid angle Ω_i and w_i is the weight of the mask at pixel i . For the four bandpowers at $\ell \leq 300$ plotted in Fig. 8, the errors are dominated by uncertainties in the dust cleaning. For these band powers we replace the elements of the covariance matrix $M_{b,b}$, $M_{b,b+1}$, $M_{b+1,b}$ for $b \leq 4$ with the covariance matrix determined from the scatter of ΔD_ℓ within the bands. The $\pm 1\sigma$ error bars plotted in Fig. 8 are computed from the diagonals of the final bandpower covariance matrix $M_{bb'}$.

The aim of this analysis is to create a simple linear combination of *Planck* spectra for which the main contaminant to the tSZ spectrum has a known spectral shape. Having subtracted the primary CMB¹⁴ and Galactic dust emission, the only significant remaining contributions to the $100 \times 100 - 143 \times 217$ spectrum come from the tSZ effect

and Poisson point sources. We model the tSZ effect using the dashed line of Fig. 1 as a template multiplied by the parameter $A_{\text{tSZ}}^{\text{Planck}}$. The radio source contribution is modeled as a Poisson spectrum with amplitude

$$D_\ell^{\text{PS}} = 31.71 A_{\text{PS}}^{\text{Planck}} \frac{\ell(\ell+1)}{10^6} \mu\text{K}^2, \quad (11)$$

where the coefficient has been chosen so that $A_{\text{PS}} = 1$ corresponds to the best fit to the $100 \times 100 - 143 \times 217$ spectrum. The relative calibration of the *Planck* TT spectra is sufficiently accurate that there is no need to sample over calibration parameters (see EG21, Section 9.1.1).

We assume a Gaussian likelihood for the bandpowers with covariance matrix $M_{bb'}$ computed as described above and sample over the two free parameters $A_{\text{tSZ}}^{\text{Planck}}$ and $A_{\text{PS}}^{\text{Planck}}$ using the **MULTINEST** nested sampler (Feroz et al. 2009, 2011). We find

$$\left. \begin{aligned} A_{\text{tSZ}}^{\text{Planck}} &= 0.706 \pm 0.243, \\ A_{\text{PS}}^{\text{Planck}} &= 1.000 \pm 0.140. \end{aligned} \right\} \quad (12)$$

These two parameters are highly correlated as illustrated in Fig. 9.

As is evident from Fig. 8, the unresolved tSZ contribution is a small effect that is difficult to measure accurately from the *Planck* data. The result of Eq. 12 has such a large error that we cannot exclude the **FLAMINGO** prediction of Fig. 1. Our results also suggest that the errors on the B18 tSZ power spectrum (and on the power spectra inferred from similar analyses of y-maps such as Tanimura et al. (2022)) have been underestimated because they do not include errors in the shapes of the major contaminants.¹⁵

The degeneracy between $A_{\text{tSZ}}^{\text{Planck}}$ and $A_{\text{PS}}^{\text{Planck}}$ can be broken by using source counts at 100 GHz. The red points in Fig. 10 show 100 GHz source counts measured by *Planck* as listed in Table 7 of Planck Collaboration et al. (2013). The blue points show the source counts at 95 GHz from the 2500 square degree SPT-SZ survey (Everett et al. 2020). We apply a small correction to the SPT flux densities in the 95 GHz band (effective frequency of 93.5 GHz for a radio source with spectral index $S_\nu \propto \nu^{\alpha_R}$, $\alpha_R \approx -0.5$) to transform to the *Planck* band frequency at 100 GHz (effective frequency of 100.84 GHz¹⁶), giving $S_{100}^{\text{Planck}} = 0.963 S_{95}^{\text{SPT}}$.

We fit the number counts shown in Fig. 10 to the function

$$S^{2.5} \frac{dN}{dS} = A_c \left(\frac{x}{100} \right)^{\alpha_c} \left(1 + \left(\frac{x}{x_c} \right)^{\beta_c} \right)^{\gamma_c}, \quad x = 1000S, \quad (13)$$

using **MULTINEST**. The marginalized posteriors of the parameters are found to be

$$\left. \begin{aligned} A_c &= 8.55 (8.51) \pm 0.35 \text{ Jy}^{1.5} \text{sr}^{-1}, \\ x_c &= 1565 (1101) \pm 420, \\ \alpha_c &= 0.419 (0.421) \pm 0.025, \\ \beta_c &= 3.63 (6.73) \pm 1.65, \\ \gamma_c &= 0.307 (0.098) \pm 0.177, \end{aligned} \right\} \quad (14)$$

where the numbers in brackets give the best fit values of the

¹⁴ Including the small frequency independent contribution from the kinetic Sunyaev-Zeldovich effect.

¹⁵ For example, Tanimura et al. (2022) use the Maniyar et al. (2021) theoretical models which are untested at frequencies below 217 GHz.

¹⁶ Interpolating between the numbers given in Planck Collaboration et al. (2014a) to $\alpha_R = -0.5$.

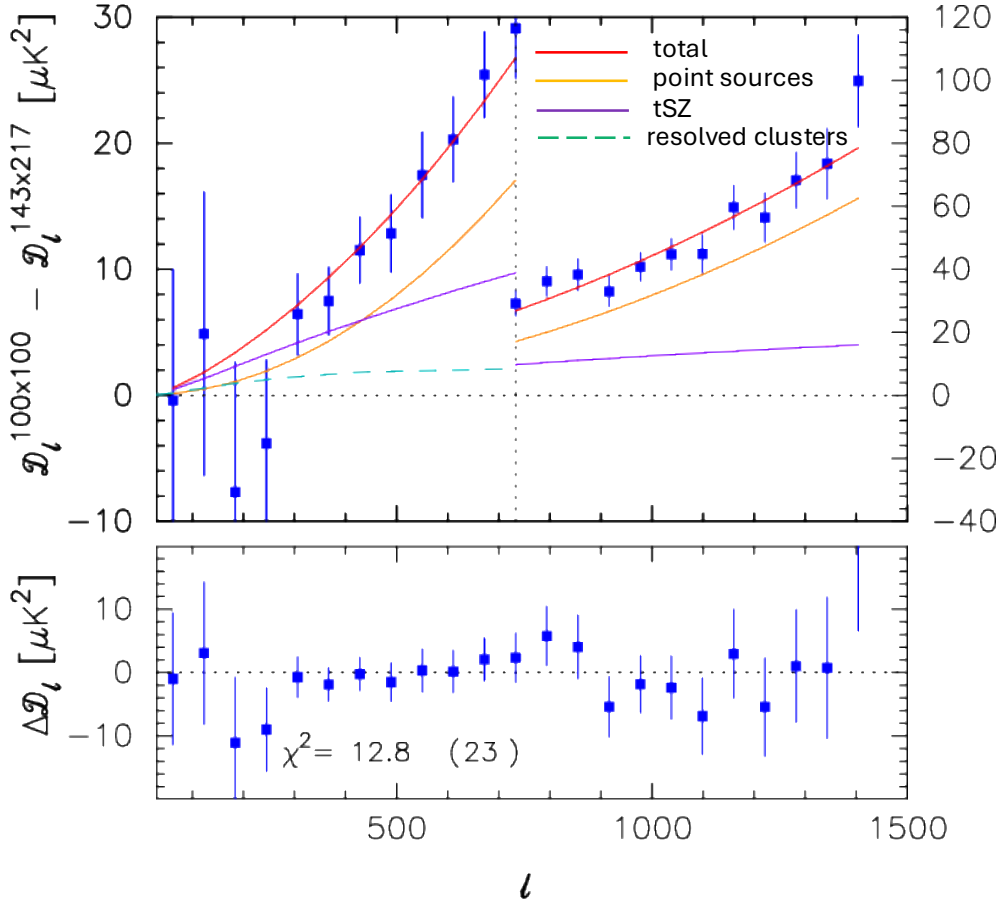


Figure 8. The upper panel shows the difference of the two spectra plotted in Fig. 7 with $\pm 1\sigma$ errors computed from the bandpower covariance matrix $M_{bb'}$, discussed in the text. The tSZ signal from clusters and the Poisson contribution from radio sources are the only significant expected contributors to the blue points. The red line in the upper panel shows the best fit foreground model which is composed of a Poisson radio source component (orange) and a tSZ component (purple) which is modeled as a template with the shape of the dashed curve in Fig. 1 with a free amplitude. The green dashed line shows the expected contribution from clusters of galaxies resolved by *Planck* (from Planck Collaboration et al. (2016a)). Note that the Coma cluster was masked in our analysis. Note also the change in the scale of the ordinate in the upper panel at $\ell = 733$. The residuals after subtraction of the foreground model are plotted in the lower panel. We list χ^2 for this fit for 23 bandpowers.

parameters. The best fit and $\pm 1\sigma$ error bars computed from the MULTINEST chains are plotted in Fig. 10.

The power spectrum of Poisson distributed point sources is given by

$$C_\ell^{\text{PS}} = \int_0^{S_{\text{lim}}} S^2 \frac{dN}{dS} dS. \quad (15)$$

Applying the monochromatic conversion from Jy to thermodynamic temperature,

$$\Delta T = \frac{(e^x - 1)^2}{x^2 e^x} \frac{c^2 I_\nu}{2\nu^2 k}, \quad x = \frac{h\nu}{kT}, \quad (16)$$

the point source amplitude at $\ell = 1000$ at 100 GHz in temperature units is given by

$$D_{1000}^{\text{PS}} = (0.00413)^2 \frac{10^6}{2\pi} \int_0^{S_{\text{lim}}} S^2 \frac{dN}{dS} dS \mu K^2. \quad (17)$$

We evaluate this integral for $S_{\text{lim}} = 400$ mJy and monitor D_{1000}^{PS} as a derived parameter in the MULTINEST chains. The

results give

$$D_{1000}^{\text{PS}} = 29.2 \pm 1.8 \mu K^2, \quad (18)$$

which is reassuringly close to the best fit value of Eq. 11 determined by fitting to the power spectrum. The point source amplitude determined from the number counts breaks the degeneracy between $A_{\text{tSZ}}^{\text{Planck}}$ and $A_{\text{PS}}^{\text{Planck}}$ as shown in Fig. 9 and favours values of A_{tSZ} close to unity. This is illustrated by the blue contours in Fig. 9 in which we have imposed the number count constraint of Eq. 18 as a prior on $A_{\text{PS}}^{\text{Planck}}$. In this case we find

$$\left. \begin{aligned} A_{\text{tSZ}}^{\text{Planck}} &= 0.815 \pm 0.128, \\ A_{\text{PS}}^{\text{Planck}} &= 0.931 \pm 0.052. \end{aligned} \right\} \text{ including PS prior.} \quad (19)$$

In summary, we have focussed on the 100 GHz *Planck* band. At this frequency, the power spectrum of radio sources, which has a known spectral shape, is the main contaminant to the tSZ signal after subtraction of the primary CMB. Our main conclusion, evident from Fig. 9, is that

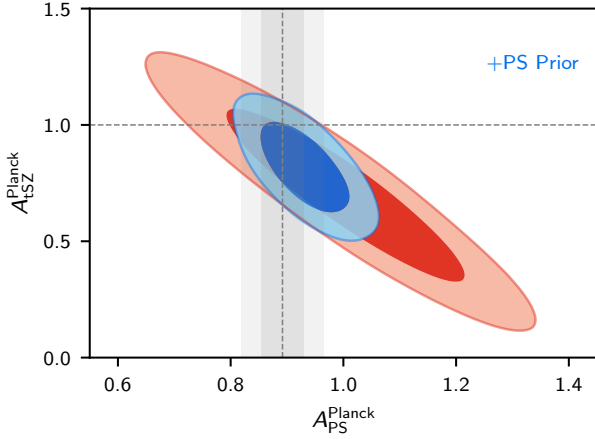


Figure 9. 68% and 95% contours on the parameters A_{tSZ}^{Planck} and A_{PS}^{Planck} derived by fitting the $100 \times 100 - 143 \times 217$ power spectrum difference (red contours). Consistency with the predictions of the FLAMINGO Λ CDM prediction of Fig. 1 requires $A_{tSZ}^{\text{Planck}} = 1$ (shown by the dotted horizontal line). The vertical bands show the 1 and 2σ constraints on A_{PS}^{Planck} derived from fitting point source number counts at 100 GHz (see Fig. 10). Blue contours show the results when the number count constraint on A_{PS}^{Planck} is included as a prior.

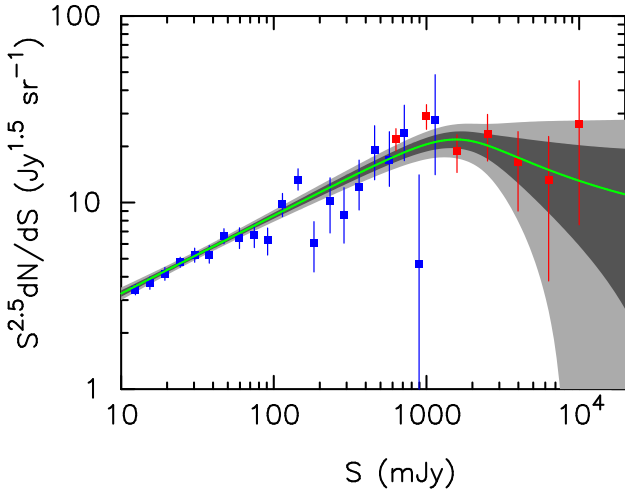


Figure 10. Source counts at 100 GHz. The red points show source counts measured from *Planck* (Planck Collaboration et al. 2013). The blue points show counts from SPT (Everett et al. 2020) at 95 GHz rescaled to 100 GHz. The green line shows the best fit to the function of Eq. 13 and the grey bands show 1 and 2σ errors computed from the MULTINEST chains.

it is difficult to make an accurate measurement of the tSZ amplitude from *Planck* even if we apply the point source prior of Eq. 18. the constraint on A_{tSZ}^{Planck} cannot exclude the FLAMINGO Λ CDM prediction shown in Fig. 1. It must be noted, however, that most of the statistical weight in Eq. 19 comes from multipoles $\ell \sim 300 - 500$. *Planck* has little sensitivity to the tSZ spectrum at higher multipoles. This will

become clearer in Sec. 4.3 where we present the results of a template-free tSZ power spectrum reconstruction.

4.2 Analysis of ACT and SPT spectra

Figure 1 shows a large discrepancy between the predictions of the FLAMINGO Λ CDM tSZ spectrum and the amplitude inferred from ACT and SPT at high multipoles. As mentioned above, the ACT and SPT constraints are derived by fitting a parametric model to power spectra over the frequency range $\sim 95 - 220$ GHz. These models include templates for a number of foreground components including the clustered CIB, which we have emphasised, is poorly known at these frequencies. In this section, we focus attention on the power spectra measured from the SPT-SZ and SPTpol surveys reported by Reichardt et al. (2021) (hereafter R21) and the ACT deep surveys reported by Choi et al. (2020) (hereafter C20). As in the previous section, our aim is to simplify the analysis so that the inferred tSZ power spectrum is insensitive to the CIB. We therefore restrict the analysis to R21 95 GHz and C20 98 GHz spectra (thus excluding the R21 150 and 220 GHz and C20 150 GHz spectra). As in the *Planck* analysis, the tSZ effect has the largest contrast relative to other foreground components in the ACT and SPT spectra at these frequencies¹⁷ (see e.g. Fig. 2 of R21).

We use the public releases of the R21 and C20 bandpowers, window functions, beam and bandpower covariance matrices¹⁸ and fit the bandpowers to a model consisting of the best fit Λ CDM power spectrum from RGE22, the FLAMINGO tSZ template (dashed line in Fig. 1) with free amplitudes A_{tSZ}^{SPT} , A_{tSZ}^{ACT} , and Poisson point source components with amplitudes

$$D_{\ell}^{\text{PS}} = \begin{cases} 7.71 A_{PS}^{\text{SPT}} \ell(\ell+1)/9 \times 10^{-6} \mu\text{K}^2, & \text{SPT,} \\ 16.25 A_{PS}^{\text{ACT}} \ell(\ell+1)/9 \times 10^{-6} \mu\text{K}^2, & \text{ACT.} \end{cases} \quad (20)$$

The coefficients in Eq. 20 are chosen so that A_{PS}^{SPT} and A_{PS}^{ACT} are close to unity for the best fits described below. We allow relative calibration coefficients c^{SPT} and c^{ACT} between *Planck* and SPT and ACT spectra, such that $c^{\text{SPT/ACT}} D_{\ell}^{\text{SPT/ACT}} = D_{\ell}^{\text{Planck}}$, which we include in the likelihood by imposing Gaussian priors on c^{SPT} and c^{ACT} with means of unity and dispersions of 0.6% (SPT) and 1% (ACT)¹⁹. We form likelihoods as described in R21 and C20 and use MULTINEST to sample over the free parameters. We find

$$\left. \begin{aligned} c^{\text{SPT}} &= 1.0057 \pm 0.0054, \\ A_{tSZ}^{\text{SPT}} &= 0.297 \pm 0.023, \\ A_{PS}^{\text{SPT}} &= 1.000 \pm 0.051, \end{aligned} \right\} \quad (21)$$

¹⁷ C20 also analyse data from a wide field survey. We do not use the wide data here because the point source contribution to the power spectrum at 98 GHz has a much higher amplitude compared to the deep survey. The wide survey is therefore much less sensitive to the tSZ effect compared to the deep survey.

¹⁸ Downloaded from

<http://pole.uchicago.edu/public/data/reichardt20/>

https://lambda.gsfc.nasa.gov/product/act/act_dr4_likelihood_get.html

¹⁹ Note that relative calibration of *Planck* and SPT at the map level leads to an uncertainty of 0.33% in power (see Sect. 2.2 of R21) and to an uncertainty of 1% in power for ACT (see Sect. 7.1 of C20).

and

$$\left. \begin{aligned} c^{\text{ACT}} &= 0.9918 \pm 0.0082, \\ A_{\text{tSZ}}^{\text{ACT}} &= 0.463 \pm 0.096, \\ A_{\text{PS}}^{\text{ACT}} &= 1.003 \pm 0.139. \end{aligned} \right\} \quad (22)$$

The differences between the SPT and ACT and power spectra and the *Planck* best fit model are shown in the upper panels of each of Figs. 11(a, b) together with the best fit foreground model. The residuals with respect to the best fit foreground model are shown in the lower panels. The low values of $A_{\text{tSZ}}^{\text{SPT}}$ and $A_{\text{tSZ}}^{\text{ACT}}$ are particularly striking because they exclude the FLAMINGO Λ CDM model at very high significance. These results are qualitatively consistent with the estimates of the tSZ amplitudes from SPT and ACT plotted in Fig. 1.

We note the following points:

(i) We have neglected the kinetic Sunyaev-Zeldovich (kSZ) effect. The analysis of multifrequency power spectra show that it is a small effect (e.g. Reichardt et al. 2012; Planck Collaboration et al. 2020b; Choi et al. 2020; Reichardt et al. 2021) with an amplitude that is highly model dependent. For example, Reichardt et al. (2012) in their analysis of two years of observation with SPT, derived the joint constraint:

$$D_{3000}^{\text{tSZ}_{150}} + 0.5D_{3000}^{\text{kSZ}_{150}} = 4.60 \pm 0.63 \mu\text{K}^2, \quad (23a)$$

for the amplitudes at $\ell = 3000$ of the tSZ and kSZ power spectra measured at 150 GHz. Choi et al. (2020) find

$$D_{3000}^{\text{tSZ}_{150}} = 5.29 \pm 0.66 \mu\text{K}^2, \quad D_{3000}^{\text{kSZ}_{150}} < 1.8 \mu\text{K}^2 (95\%), \quad (23b)$$

while Reichardt et al. (2021) find

$$D_{3000}^{\text{tSZ}_{150}} = 3.42 \pm 0.54 \mu\text{K}^2, \quad D_{3000}^{\text{kSZ}_{150}} = 3.0 \pm 1.0 \mu\text{K}^2, \quad (23c)$$

and that the tSZ and kSZ amplitudes are correlated as a consequence of the tSZ-CIB cross-correlation (which is very poorly known, see e.g. Addison et al. (2012)). The correlation from Fig. 3 of R21 is well approximated by $D_{3000}^{\text{tSZ}_{150}} + 0.5D_{3000}^{\text{kSZ}_{150}} \approx 5 \mu\text{K}^2$, consistent with Eq. 23a. We will refer to the results in Eqs. 23b and 23c as the ACT and SPT SZ measurements respectively.

(ii) The tSZ amplitudes of Eq. 21 and 22 correspond to amplitudes at 95 and 98 GHz of $D_{3000}^{\text{SPT}_{95}} = 10.39 \mu\text{K}^2$ and $D_{3000}^{\text{ACT}_{98}} = 15.3 \mu\text{K}^2$. Converting the tSZ amplitudes at 150 GHz quoted in (i), we find $D_{3000}^{\text{tSZ}_{98}} = 14.26 \pm 1.8 \mu\text{K}^2$ (ACT) and $D_{3000}^{\text{tSZ}_{95}} = 9.1 \pm 1.4 \mu\text{K}^2$ (SPT). The kSZ contribution is frequency independent and, as noted above, is extremely uncertain. In our analysis, we have neglected the kSZ effect, and so our results could overestimate the amplitude of the tSZ effect by up to a few μK^2 . However, it is clear from Fig. 11 that the FLAMINGO tSZ template, which predicts $D_{3000}^{\text{tSZ}_{100}} \approx 32 \mu\text{K}^2$, is firmly excluded and cannot be reconciled with the data by any plausible changes to the primary CMB and foreground model. The Λ CDM FLAMINGO simulations are therefore strongly discrepant with observations of the tSZ effect at high multipoles.

(iii) In Sect. 4.1 we applied a prior based on point source number counts to reduce the degeneracy between A_{tSZ} and A_{PS} . Both ACT and SPT mask point sources identified at 150 GHz and so it is not possible to use source counts to predict the point source power at ~ 100 GHz without separating infrared galaxies from radio sources and making as-

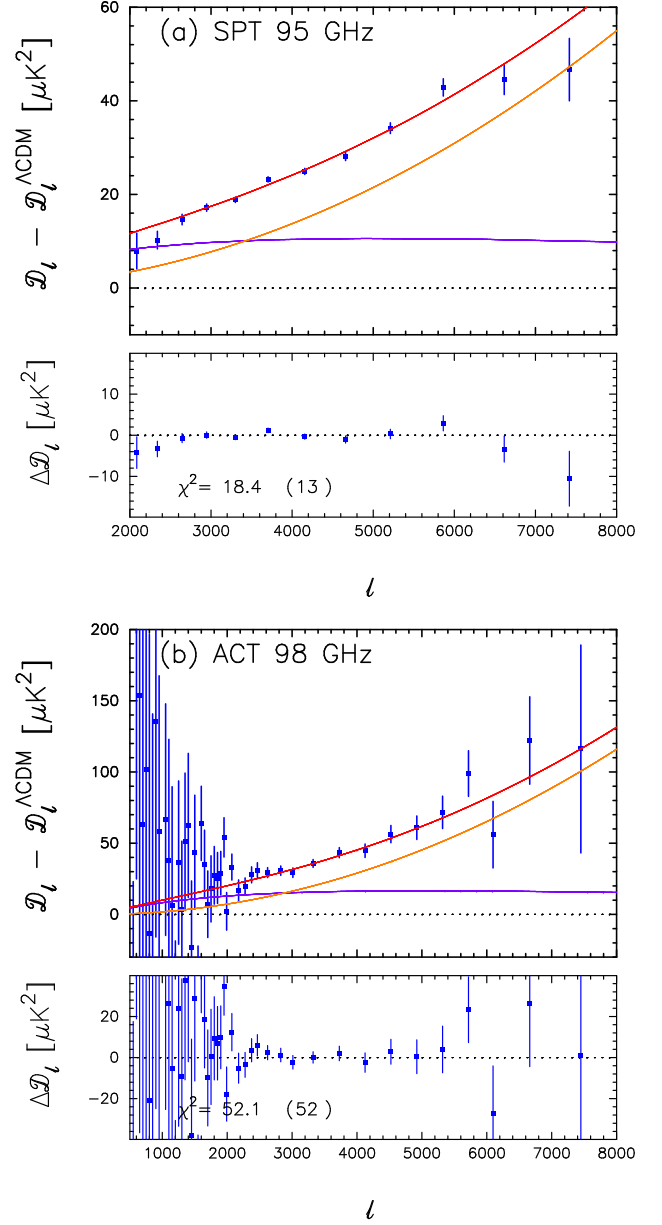


Figure 11. The upper panels in each plot show the differences between the 95 GHz SPT and 98 GHz ACT bandpowers and the power spectrum of the best fit Λ CDM cosmology from RGE21. The $\pm 1\sigma$ errors on the bandpowers were computed from the diagonals of the SPT and ACT covariance matrices. The lines show the best fit foreground model. The total foreground is shown in red, tSZ contribution is shown in purple, and the Poisson point source contribution is shown in orange. The residuals after subtraction of the foreground model are plotted in the lower panels. We list χ^2 for the best fits for 13 SPT bandpowers and 52 ACT bandpowers.

sumptions about the spectral indices of the sources. Fortunately, the tSZ amplitudes from ACT and SPT are tightly constrained without application of an external constraint on the point source amplitude.

(iv) The amplitude of the tSZ template inferred from *Planck*, which is weighted towards multipoles of $\sim 300-500$ (Fig. 8),

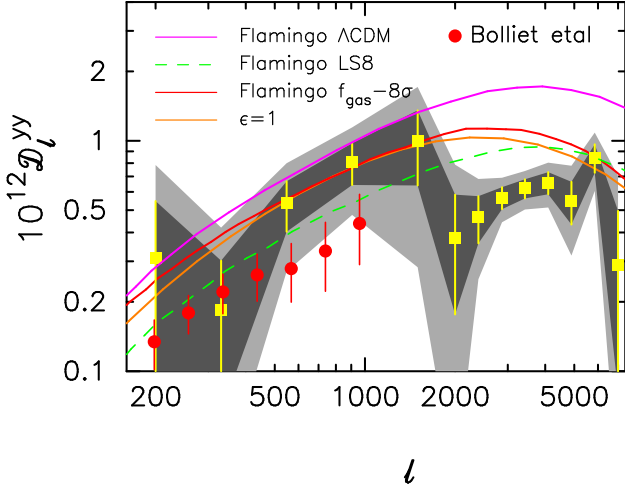


Figure 12. Reconstruction of the tSZ power spectrum derived by combining the *Planck*, ACT and SPT likelihoods of the previous subsections (yellow points). We solve for the amplitude of D^{yy} at each of 13 node points and interpolate the tSZ spectrum between the nodes shown in the Figure. The shaded bands show the 1 and 2σ errors. The red points show the tSZ spectrum inferred by B18 as plotted in Fig. 3. The curves show the baseline Λ CDM FLAMINGO prediction from Fig. 1 (purple line), results for the FLAMINGO LS8 (low S_8) model (dashed green line), a FLAMINGO simulation with enhanced baryonic feedback (red line labeled $f_{\text{gas}} - 8\sigma$, see text) and the halo model of Sect. 2 with evolution parameter $\epsilon = 1$ (orange line). The violet dashed line shows the best fit template tSZ spectrum deduced from ACT-DR6 (see Sec. 5)

is $A_{\text{tSZ}} \sim 0.8$. For ACT, which is weighted to multipoles of $\sim 2000 - 2500$ (Fig. 11b) we find $A_{\text{tSZ}} \sim 0.46$. For SPT which is weighted to multipoles of $\sim 2500 - 3500$ (Fig. 11b), we find $A_{\text{tSZ}} \sim 0.297$. These results show a trend for A_{tSZ} to decrease as we probe higher multipoles, suggesting that the true tSZ power spectrum may be shallower than the FLAMINGO template used to derive these numbers. We explore this possibility in the next subsection.

4.3 Template free analysis

In this subsection we combine the *Planck*, ACT and SPT likelihoods described above and solve for the shape of the tSZ power spectrum neglecting any contribution from the kSZ effect. The amplitudes of the spectrum $D_{\ell_{\text{node}}}^{yy}$ at a set of node points ℓ_{node} are treated as free parameters. The tSZ spectrum in between node points is computed by linear interpolation in $\log_{10} \ell$. The node points are specified in Table 1. We then run MULTINEST to solve for the 13 amplitudes $D_{\ell_{\text{node}}}^{yy}$, 3 point source amplitudes $A_{\text{PS}}^{\text{Planck}}$, $A_{\text{PS}}^{\text{ACT}}$, $A_{\text{PS}}^{\text{SPT}}$, with a number count prior on $A_{\text{PS}}^{\text{Planck}}$ as described in Sect. 4.1, and two calibration parameters c^{ACT} and c^{SPT} with Gaussian priors as discussed in Sect. 4.2.

The results are summarized in Table 1 and in Fig. 12. The constraints from *Planck* are tightest at $\ell \sim 500$ and flare out at lower and higher multipoles. The reconstructed power spectrum shows a dip at $\ell \sim 2000$ which comes from the lowest two band powers in the SPT spectrum plotted in

Table 1. Reconstruction of the tSZ power spectrum using *Planck*, ACT and SPT power spectra. The first column gives the value of the multipole at each of 13 nodes. The second column gives the estimate of the yy power spectrum at each node point. The tSZ spectrum is interpolated linearly in $\log_{10} \ell$ between these nodes. The third column gives the 1σ error on $10^{12} D_{\ell_{\text{node}}}^{yy}$.

ℓ_{node}	$10^{12} D_{\ell_{\text{node}}}^{yy}$	1σ error
200.	0.310	0.237
330.97	0.184	0.118
547.72	0.535	0.132
906.4	0.810	0.166
1500.	0.997	0.357
2000.	0.380	0.204
2391.96	0.467	0.108
2869.74	0.567	0.0619
3421.38	0.621	0.0591
4091.91	0.659	0.073
4893.84	0.548	0.114
5852.94	0.846	0.120
7000.	0.289	0.207

Fig. 11a. The best fit to the ACT 98 GHz spectrum actually shows a small excess at $\ell \sim 2000$ (see Fig. 11b) but the ACT spectra contribute relatively low statistical weight compared to *Planck* and SPT. The results appear to show a jump in power at $\ell \sim 2000$, but it is important to recognise that the *Planck* points are strongly correlated and can move in lock-step towards the top or bottom of the error ranges depending on the amplitude of the radio point source amplitude. We also show the points from B18, which lie at the bottom end of the $\sim 2\sigma$ error range for our measurements. Continuity with the results from ACT and SPT suggests that the true amplitude of the tSZ spectrum at $\ell \lesssim 1000$ lies at the lower end of the error range. Overall, the results shown in Fig. 12 show a large discrepancy at high multipoles with the baseline Λ CDM FLAMINGO prediction at $\ell \gtrsim 2000$. In addition, the amplitude D^{yy} inferred from *Planck* at $\ell \sim 500$ is similar to the amplitude inferred at $\ell \sim 3000$, thus the tSZ spectrum must have a shallower slope than the baseline Λ CDM FLAMINGO prediction. We defer further interpretation of these results to the next Section.

5 DISCUSSION AND CONCLUSIONS

The aim of this paper has been to present an alternative (and transparent) way of measuring the tSZ power spectrum compared to the usual approach based on y-maps. As discussed in Sect. 3, all y-maps are contaminated by other components and require assumptions concerning the shapes of their power spectra to extract a tSZ power spectrum.

In this paper, we have concentrated on fitting temperature power spectra at 100 GHz, where the dominant contributions come from the primary CMB, tSZ and radio point sources. The latter component can be modeled accurately by a Poisson power spectrum $D_{\ell}^{PS} \propto \ell^2$. We do not consider higher frequencies since they require an accurate model of the CIB, and also the cross-correlation of the tSZ signal with the CIB, in order to extract the subdominant tSZ signal.

The tSZ power spectrum that we infer from *Planck* is

consistent with those inferred from *Planck* y-maps (B18, Tanimura et al. (2022)) but has larger errors, which we believe are more realistic. As a consequence, our analysis of *Planck* cannot exclude the FLAMINGO Λ CDM tSZ spectrum.

However, a similar analysis applied to the ACT 98 GHz and SPT 95 GHz provides convincing evidence of a large discrepancy with the FLAMINGO model at multipoles $\ell \gtrsim 2000$. The results from ACT and SPT spectra are consistent with each other and also with earlier analyses of ACT and SPT (Reichardt et al. 2012; Dunkley et al. 2013). The low amplitude of the tSZ spectrum at high multipoles is therefore a robust result and must be reproduced in cosmological hydrodynamical simulations that claim to match reality. We consider the following two possibilities to explain the discrepancy:

(A) A low value of S_8

As noted in Sects. 1 and 2, the amplitude of the tSZ spectrum is sensitive to value of the S_8 parameter quantifying the amplitude of the mass fluctuation spectrum. Motivated by indications of a low value of S_8 from cosmic shear surveys, M23 ran a set of simulations (labelled LS8) of a Λ CDM cosmology, but with the amplitude of the fluctuation spectrum lowered to give $S_8 = 0.766$ (corresponding to the low S_8 ‘cosmic shear’ cosmology discussed by Amon et al. (2023)). The tSZ spectrum of the FLAMINGO LS8 cosmology is plotted in Fig. 12. At $\ell = 2780$, the LS8 model predicts $10^{12} D_{2780}^{yy} = 0.90$, whereas the measured value from Table 1 is 0.57 ± 0.062 (which may be an overestimate since we have neglected the kSZ effect). For comparison, the FLAMINGO *Planck* Λ CDM prediction is $10^{12} D_{2780}^{yy} = 1.69$. The scaling between these two predictions is in good agreement with Eq. 4. To match the ACT/SPT tSZ amplitude would require a value of $S_8 \sim 0.73$, which is lower than inferred from cosmic shear surveys (e.g. Dark Energy Survey and Kilo-Degree Survey Collaboration et al. 2023).

Furthermore, a number of new measurements sensitive to linear scales have been reported which disfavour a low S_8 cosmology, as summarized in Table 2. The *Planck* lensing and ACT DR6 measurements give values of S_8 that are in excellent agreement with the values inferred from the *Planck* temperature and polarization measurements (entries [1]–[3]). The CMB lensing measurements are sensitive to the mass distribution over a broad range of redshifts peaked at $z \sim 2$. The redshift range can be sharpened by cross-correlating CMB lensing with galaxy surveys. Entries [4]–[7] report results cross-correlating ACT and *Planck* lensing measurements with the unWISE catalogue of infrared galaxies (Schlafly et al. 2019) and the DESI Luminous Red Galaxy (LRG) sample. The final entry [8] summarizes the results of the full shape modeling of galaxy and quasar clustering from the first year DESI observations, which is sensitive to S_8 via redshift space distortions. Measurements [4], [6] and [8] are largely independent and if combined give $S_8 = 0.798 \pm 0.014$, which is within 1.5σ of the *Planck* TTTEEE value in entry [1]. It therefore seems extremely unlikely that a low value of S_8 is the reason that the FLAMINGO simulations fail to match the ACT/SPT tSZ measurements.

(B) Enhanced Baryonic Feedback

Another possibility is that baryonic feedback is much more important than modeled in the baseline FLAMINGO sim-

ulations.²⁰ The red line in Fig. 12 shows results from a FLAMINGO simulation with strong baryonic feedback (McCarthy et al. 2024). For this model, the AGN feedback prescription was adjusted so that the gas fractions in groups are 8σ lower than in the baseline model (hence the designation $f_{\text{gas}} - 8\sigma$). Even in this case, the model fails to match the low tSZ power inferred from ACT and SPT. The orange line in Fig. 12 shows a model with the self-similar evolution parameter of Eq. 11 set to $\epsilon = 1$. This also fails to match the ACT/SPT measurements.

There is however evidence to support the idea that the baseline FLAMINGO simulations are underestimating the effects of baryonic feedback. *Planck*+ACT measurements stacked on galaxy reconstructed velocities derived from the Baryon Oscillation Spectroscopic Survey (Schaan et al. 2021) leads to a kSZ signal favouring higher levels of baryonic feedback than in the baseline FLAMINGO simulations (Bigwood et al. 2024; McCarthy et al. 2024). Evidence for high levels of baryonic feedback has been presented by (Hadzhiyska et al. 2024) from a similar kSZ analysis using ACT maps stacked on DESI LRGs using photometric redshifts to infer the velocity field. We also note that cosmic shear tSZ cross-correlation measurements suggest that high levels of baryonic feedback are required to reconcile a *Planck* Λ CDM cosmology with observations (Tröster et al. 2022; Pandey et al. 2023; McCarthy et al. 2023; Posta et al. 2024). However, despite these results it remains an open question of whether baryonic feedback can explain tSZ spectrum at high multipoles deduced from ACT and SPT.

Finally, we note that the tSZ power spectrum has been used in many papers to constrain cosmology, largely neglecting the role of baryonic feedback (e.g. *Planck* Collaboration et al. 2016b; Hurier & Lacasa 2017; Salvati et al. 2018; Tanimura et al. 2022, 2023). The results presented here suggest that baryonic feedback is an essential ingredient in shaping the tSZ spectrum and cannot be ignored.

We note that two papers have appeared while this paper was in the final stages of revision: (i) The KiDS collaboration has published results on cosmic shear from the KiDS-Legacy Survey (Wright et al. 2025) which surveys 1347 square degrees and extends the redshift reach to redshift 2. Improvements in the photometric redshifts and various other aspects of the cosmic shear analysis lead to a shift in the S_8 measurement compared to earlier KiDS results with the new analysis finding $S_8 = 0.815^{+0.016}_{-0.021}$, consistent with the *Planck* Λ CDM value quoted in Table 2. This result strengthens the conclusion that the observed tSZ spectrum cannot be explained by invoking a low value of S_8 ; (ii) the ACT collaboration have published power spectra from ACT DR6 (Louis et al. 2025) at frequencies of 98, 150 and 220 GHz. They solve for a tSZ contribution to the temperature power spectra as in earlier papers (Choi et al. 2020) using the tSZ template power spectrum ℓ^{bat} from Battaglia et al. (2012). With the increased signal-to-noise of the ACT DR6 data they are able to solve for a shape parameter α_{tSZ} ,

²⁰ The first version of this paper compared the empirical results shown in Fig. 12 with halo models of the tSZ spectrum from Omori (2024) which attempted to model enhanced baryonic feedback. However, the Omori (2024) models do not reproduce the tSZ spectra measured directly from the simulations on which the models are based (see Fig. 6 of McCarthy et al. (2018)).

Table 2. Measurements of S_8 assuming the base Λ CDM cosmology.

	Data	S_8	reference
[1]	Planck TTTEEE	0.828 ± 0.013	Efstathiou & Gratton (2021)
[2]	Planck TTTEEE+Planck lensing	0.829 ± 0.012	Efstathiou & Gratton (2021)
[3]	ACT lensing+BAO	0.840 ± 0.028	Madhavacheril et al. (2024)
[4]	ACT lensing×unWISE ($z = 0.2 - 1.6$)	0.813 ± 0.021	Farren et al. (2024b)
[5]	ACT lensing+Planck lensing+unWISE 3×2 pt	0.816 ± 0.015	Farren et al. (2024a)
[6]	Planck lensing×DESI (LRG) ($z = 0.4 - 1.0$)	0.762 ± 0.024	Sailer et al. (2024)
[7]	ACT lensing×DESI (LRG) ($z = 0.4 - 1.0$)	$0.790^{+0.024}_{-0.027}$	Sailer et al. (2024)
[8]	DESI Full Shape ($z = 0.2 - 2.1$)	0.836 ± 0.035	DESI Collaboration et al. (2024)

such that $D^{yy} = a_{\text{tSZ}}^{yy} (D_{\ell}^{\text{Bat}}/D_{3000}^{\text{Bat}})(\ell/3000)^{\alpha_{\text{tSZ}}}$. They find $a_{\text{tSZ}}^{yy} = 0.49 \pm 0.06$ and $\alpha_{\text{tSZ}} = -0.6 \pm 0.2$. Their best fit is plotted as the violet dashed line in Fig. 12 and is consistent with the results presented in this paper. It would be interesting to perform a reconstruction of the tSZ spectrum using ACT-DR6. The agreement of our results with ACT-DR6 emphasises the need for further research to establish whether barionic feedback can lead to a tSZ power spectrum with the amplitude and shape shown in Fig. 12.

6 ACKNOWLEDGEMENTS

GPE is grateful to the Leverhulme Foundation for the award of a Leverhulme Emeritus Fellowship. FMCC acknowledges support from the European Research Council (ERC) under the European Union’s Horizon 2020 research and innovation programme (Grant agreement No. 851274). The Flatiron Institute is a division of the Simons Foundation. We thank Alex Amon, Leah Bigwood, Boris Bolliet, Will Coulton, Colin Hill, Hiranya Peiris, Calvin Preston, Joop Schaye and Debora Sijacki, for many useful discussions concerning this work. We thank the referee for their comments on the manuscript.

DATA AVAILABILITY

No new data were generated or analysed in support of this research.

REFERENCES

Addison G. E., Dunkley J., Spergel D. N., 2012, *MNRAS*, **427**, 1741
Ade P., et al., 2019, *J. Cosmology Astropart. Phys.*, **2019**, 056
Amon A., Efstathiou G., 2022, *MNRAS*, **516**, 5355
Amon A., et al., 2022, *Phys. Rev. D*, **105**, 023514
Amon A., et al., 2023, *MNRAS*, **518**, 477
Arnaud M., Pratt G. W., Piffaretti R., Böhringer H., Croston J. H., Pointecouteau E., 2010, *A&A*, **517**, A92
Asgari M., et al., 2021, *A&A*, **645**, A104
Battaglia N., Bond J. R., Pfrommer C., Sievers J. L., 2012, *ApJ*, **758**, 75
Béthermin M., et al., 2012, *ApJ*, **757**, L23
Bigwood L., et al., 2024, *MNRAS*, **534**, 655
Bleem L. E., et al., 2022, *ApJS*, **258**, 36
Bolliet B., Comis B., Komatsu E., Macías-Pérez J. F., 2018, *MNRAS*, **477**, 4957
Braspenning J., et al., 2023, *arXiv e-prints*, p. arXiv:2312.08277

Carlstrom J. E., Holder G. P., Reese E. D., 2002, *ARA&A*, **40**, 643
Chandran J., Remazeilles M., Barreiro R. B., 2023, *MNRAS*, **526**, 5682
Chen X., Wright E. L., 2009, *Astrophys. J.*, **694**, 222
Chluba J., Hill J. C., Abitbol M. H., 2017, *MNRAS*, **472**, 1195
Choi S. K., et al., 2020, *J. Cosmology Astropart. Phys.*, **2020**, 045
Cole S., Kaiser N., 1988, *MNRAS*, **233**, 637
Coulton W., et al., 2024, *Phys. Rev. D*, **109**, 063530
DESI Collaboration et al., 2024, *arXiv e-prints*, p. arXiv:2411.12022
Dark Energy Survey and Kilo-Degree Survey Collaboration et al., 2023, *The Open Journal of Astrophysics*, **6**, 36
Das S., et al., 2014, *J. Cosmology Astropart. Phys.*, **2014**, 014
Delabrouille J., Cardoso J. F., Le Jeune M., Betoule M., Fay G., Guillaux F., 2009, *A&A*, **493**, 835
Dunkley J., et al., 2013, *J. Cosmology Astropart. Phys.*, **2013**, 025
Efstathiou G., Gratton S., 2021, *The Open Journal of Astrophysics*, **4**, 8
Efstathiou G., Migliaccio M., 2012, *MNRAS*, **423**, 2492
Everett W. B., et al., 2020, *ApJ*, **900**, 55
Farren G. S., et al., 2024a, *arXiv e-prints*, p. arXiv:2409.02109
Farren G. S., et al., 2024b, *ApJ*, **966**, 157
Feroz F., Hobson M. P., Bridges M., 2009, *MNRAS*, **398**, 1601
Feroz F., Hobson M. P., Bridges M., 2011, MultiNest: Efficient and Robust Bayesian Inference (ascl:1109.006)
Hadzhiyska B., et al., 2024, *arXiv e-prints*, p. arXiv:2407.07152
Heymans C., et al., 2012, *MNRAS*, **427**, 146
Hikage C., et al., 2019, *PASJ*, **71**, 43
Hill J. C., Pajer E., 2013, *Phys. Rev. D*, **88**, 063526
Hill J. C., Spergel D. N., 2014, *J. Cosmology Astropart. Phys.*, **2014**, 030
Hurier G., Lacasa F., 2017, *A&A*, **604**, A71
Hurier G., Macías-Pérez J. F., Hildebrandt S., 2013, *A&A*, **558**, A118
Jenkins A., Frenk C. S., White S. D. M., Colberg J. M., Cole S., Evrard A. E., Couchman H. M. P., Yoshida N., 2001, *MNRAS*, **321**, 372
Komatsu E., Kitayama T., 1999, *ApJ*, **526**, L1
Komatsu E., Seljak U., 2002, *MNRAS*, **336**, 1256
Li Z., Puglisi G., Madhavacheril M. S., Alvarez M. A., 2022, *JCAP*, **08**, 029
Louis T., et al., 2025, *arXiv e-prints*, p. arXiv:2503.14452
MacCrann N., Zuntz J., Bridle S., Jain B., Becker M. R., 2015, *MNRAS*, **451**, 2877
Madhavacheril M. S., et al., 2020, *Phys. Rev. D*, **102**, 023534
Madhavacheril M. S., et al., 2024, *ApJ*, **962**, 113
Mak D. S. Y., Challinor A., Efstathiou G., Lagache G., 2017, *MNRAS*, **466**, 286
Maniyar A., Béthermin M., Lagache G., 2021, *A&A*, **645**, A40
McCarthy F., Hill J. C., 2024, *Phys. Rev. D*, **109**, 023528
McCarthy I. G., Le Brun A. M. C., Schaye J., Holder G. P., 2014,

- MNRAS, 440, 3645
- McCarthy I. G., Bird S., Schaye J., Harnois-Deraps J., Font A. S., van Waerbeke L., 2018, MNRAS, 476, 2999
- McCarthy I. G., et al., 2023, MNRAS, 526, 5494
- McCarthy I. G., et al., 2024, arXiv e-prints, p. arXiv:2410.19905
- Omori Y., 2024, MNRAS, 530, 5030
- Pandey S., et al., 2023, MNRAS, 525, 1779
- Planck Collaboration et al., 2013, A&A, 550, A133
- Planck Collaboration et al., 2014a, A&A, 571, A9
- Planck Collaboration et al., 2014b, A&A, 571, A16
- Planck Collaboration et al., 2016a, A&A, 594, A22
- Planck Collaboration et al., 2016b, A&A, 594, A26
- Planck Collaboration et al., 2020a, A&A, 641, A5
- Planck Collaboration et al., 2020b, A&A, 641, A6
- Planck Collaboration et al., 2020c, A&A, 643, A42
- Posta A. L., Alonso D., Chisari N. E., Ferreira T., García-García C., 2024, *X + y*: insights on gas thermodynamics from the combination of X-ray and thermal Sunyaev-Zel'dovich data cross-correlated with cosmic shear (arXiv:2412.12081), <https://arxiv.org/abs/2412.12081>
- Preston C., Amon A., Efstathiou G., 2023, MNRAS, 525, 5554
- Reichardt C. L., et al., 2012, ApJ, 755, 70
- Reichardt C. L., et al., 2021, ApJ, 908, 199
- Remazeilles M., Delabrouille J., Cardoso J.-F., 2011, Mon. Not. Roy. Astron. Soc., 410, 2481
- Rosenberg E., Gratton S., Efstathiou G., 2022, MNRAS, 517, 4620
- Sailer N., et al., 2024, arXiv e-prints, p. arXiv:2407.04607
- Salvati L., Douspis M., Aghanim N., 2018, A&A, 614, A13
- Schaan E., et al., 2021, Phys. Rev. D, 103, 063513
- Schaye J., et al., 2023, MNRAS, 526, 4978
- Schlaflly E. F., Meisner A. M., Green G. M., 2019, ApJS, 240, 30
- Secco L. F., et al., 2022, Phys. Rev. D, 105, 023515
- Shaw L. D., Zahn O., Holder G. P., Doré O., 2009, ApJ, 702, 368
- Sievers J. L., et al., 2013, J. Cosmology Astropart. Phys., 2013, 060
- Stein G., Alvarez M. A., Bond J. R., van Engelen A., Battaglia N., 2020, JCAP, 10, 012
- Sunyaev R. A., Zeldovich Y. B., 1972, Comments on Astrophysics and Space Physics, 4, 173
- Tanimura H., Douspis M., Aghanim N., Salvati L., 2022, MNRAS, 509, 300
- Tanimura H., Douspis M., Aghanim N., 2023, in Ruffino R., Vereshchagin G., eds, The Sixteenth Marcel Grossmann Meeting. On Recent Developments in Theoretical and Experimental General Relativity, Astrophysics, and Relativistic Field Theories. pp 1527–1531, doi:10.1142/9789811269776_0121
- Thorne B., Dunkley J., Alonso D., Naess S., 2017, Mon. Not. Roy. Astron. Soc., 469, 2821
- Tröster T., et al., 2022, A&A, 660, A27
- Tucci M., Toffolatti L., de Zotti G., Martínez-González E., 2011, A&A, 533, A57
- Viero M. P., et al., 2013, ApJ, 772, 77
- Wright A. H., et al., 2025, arXiv e-prints, p. arXiv:2503.19441